Electronic Supplementary Material (ESI) for Journal of Materials Chemistry A.

Supporting Information

Surfactant-assisted ZnO processing as a versatile route to ZIF composites and hollow architectures with enhanced dye adsorption

*Samir El-Hankari, Jordi Aguilera-Sigalat, Darren Bradshaw**

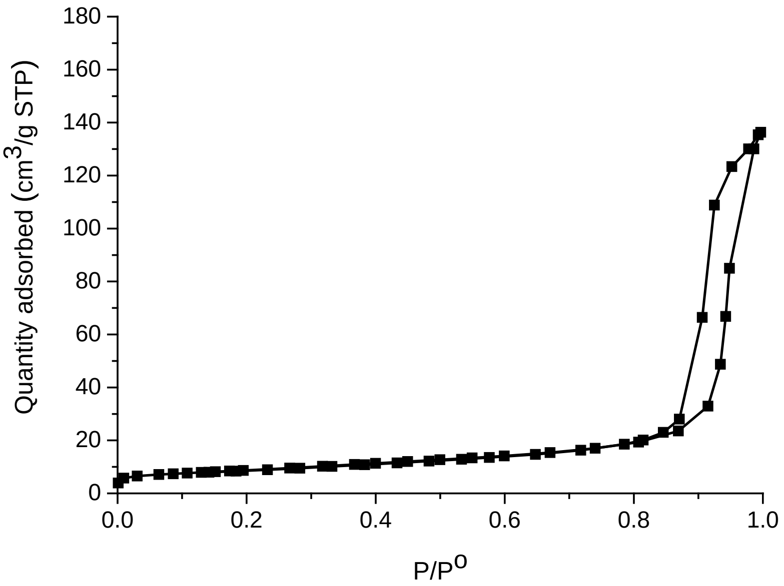

Figure S1. Nitrogen adsorption isotherm (77 K) of the as-prepared ZnO microspheres.

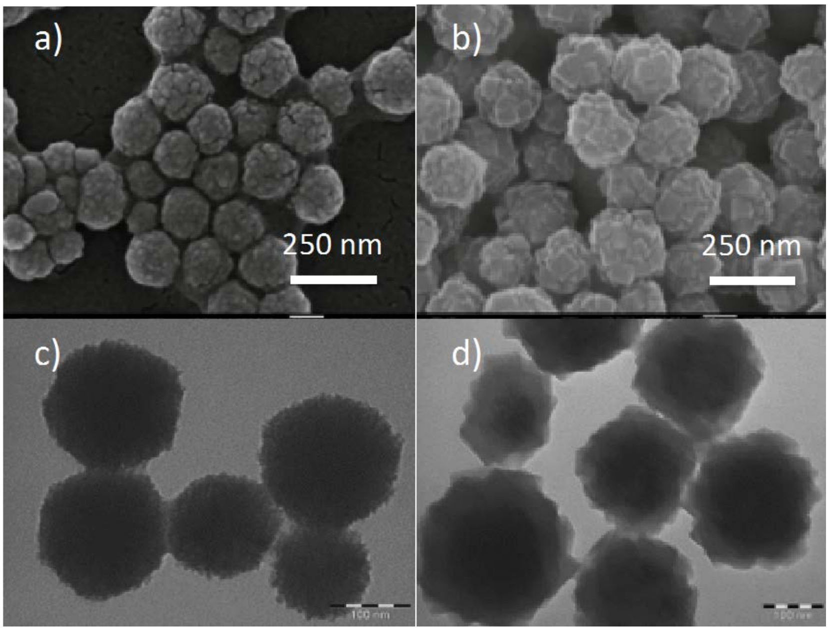

Figure S2. SEM and TEM images of ZnO nanospheres (a, c) and the resulting ZnO@ZIF-8 composites (b, d) prepared in water, clearly showing the core-shell structure of the material. Scale bars in (c) and (d) are 100 nm.

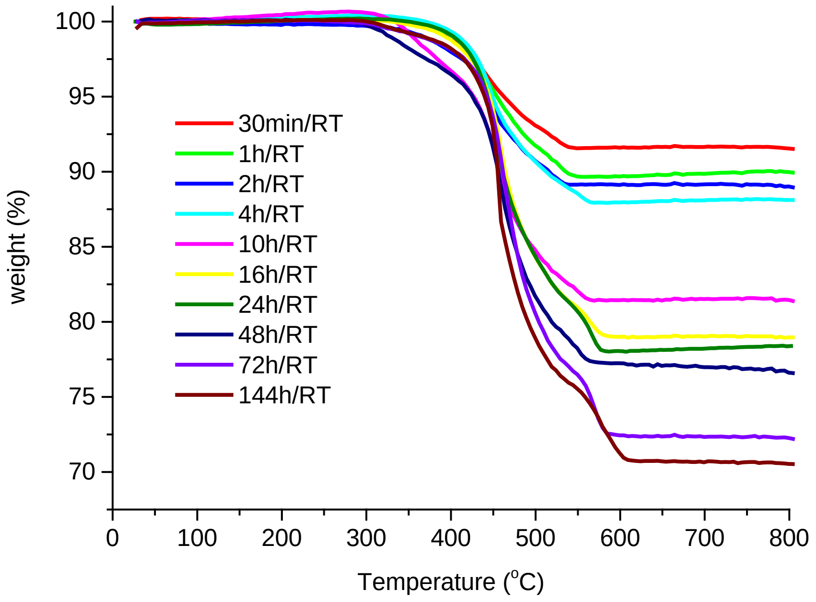

Figure S3. Thermogravimetric analysis of ZnO@ZIF-8 composite microspheres prepared in the presence of C_{12}Gua in MeOH at r.t. for various reaction times.

Sample	S_{BET}(m^2/g)	Micropore Vol (cm^3/g)[a]	Organic content from TGA (wt%)	Residual ZnO content (wt%)	ZIF-8 %	ZnO %
ZnO@ZIF-0.5h	234	0.09	8.6	91.4	13.4	86.6
ZnO@ZIF-1h	310	0.12	11	89	17.2	82.8
ZnO@ZIF-2h	409	0.16	12.3	87.7	19.2	80.8
ZnO@ZIF-4h	457	0.18	14.3	85.7	22.3	77.7
ZnO@ZIF-10h	597	0.23	19.2	80.8	30	70
ZnO@ZIF-16h	753	0.28	21.2	78.2	33.1	66.9
ZnO@ZIF-24h	870	0.31	21.9	78.1	34.2	65.8
ZnO@ZIF-48h	898	0.35	23	77	35.9	64.1
ZnO@ZIF-72h	1081	0.38	27.8	72.2	34.4	56.6
ZnO@ZIF-144h	1106	0.39	29.6	70.4	46.2	53.8

[a] Maximum pore volume at P/Po = 0.17 determined by the Horvath-Kawazoe method

Table S1. Porosity and composition data of ZnO@ZIF-8 composite microspheres prepared in the presence of C_{12}Gua in MeOH at r.t. for various reaction times. The composition is determined from the TGA data in figure S3 and the BET surface areas from the isotherms in figure S5.

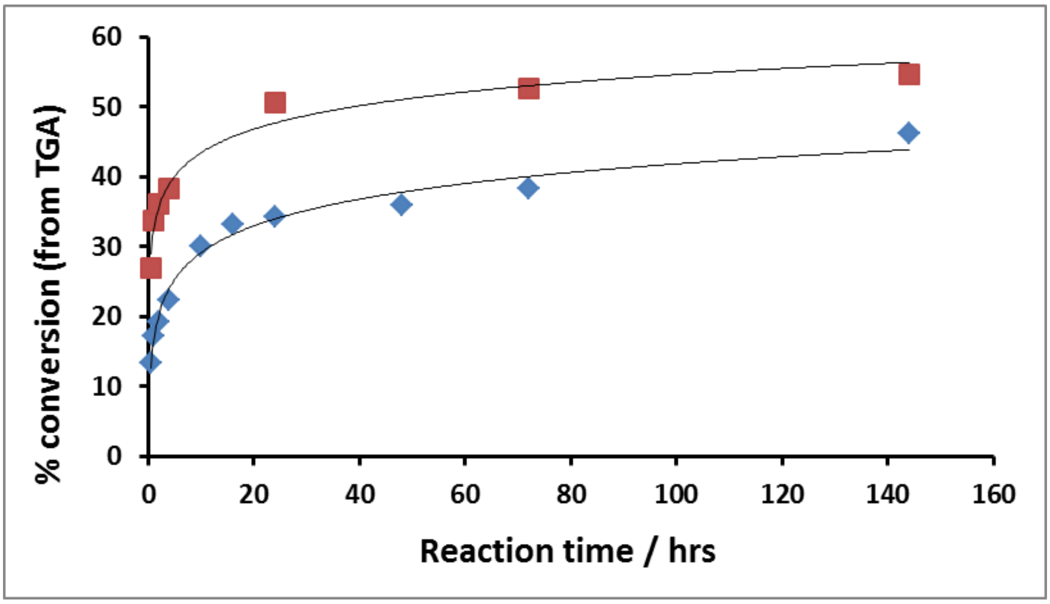

Figure S4. Conversion vs. time plot for ZnO@ZIF-8 microspheres prepared in the presence of C_{12}Gua in MeOH at r.t. (blue diamond) and 60 °C (red square).

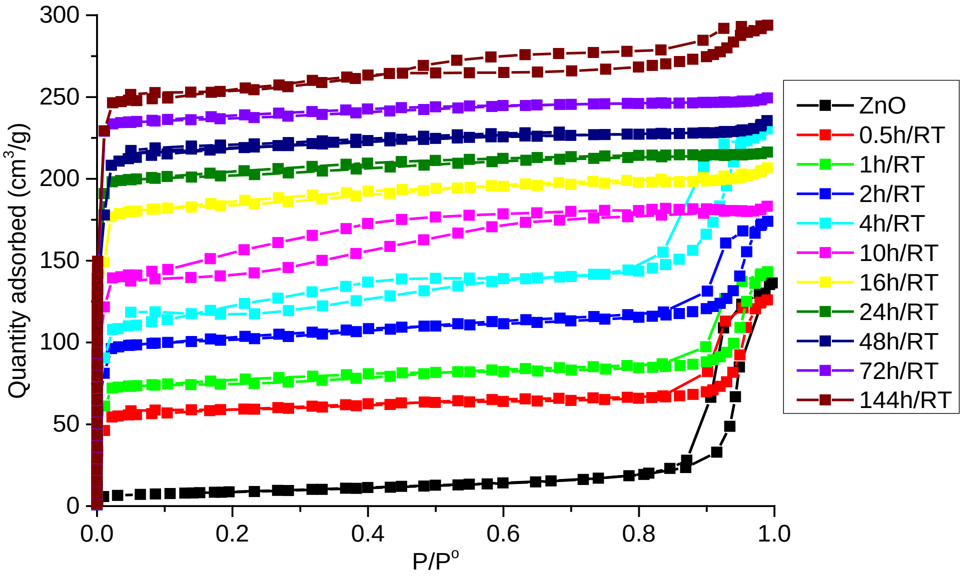

Figure S5. Nitrogen adsorption isotherm (77 K) of ZnO@ZIF-8 composite microspheres prepared in the presence of C_{12}Gua in MeOH at r.t. for various reaction times, compared to the starting ZnO. Nitrogen uptake into framework micropores, and thus ZIF-8 proportion in the composite, increases with reaction time.

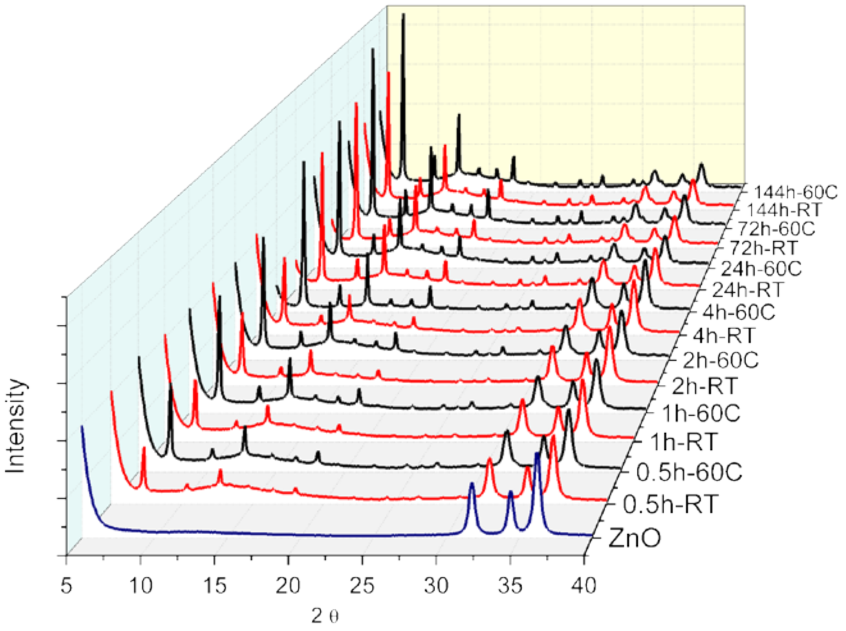

Figure S6. PXRD data of ZnO@ZIF-8 composite microspheres prepared in MeOH at 60 °C for various reaction times.

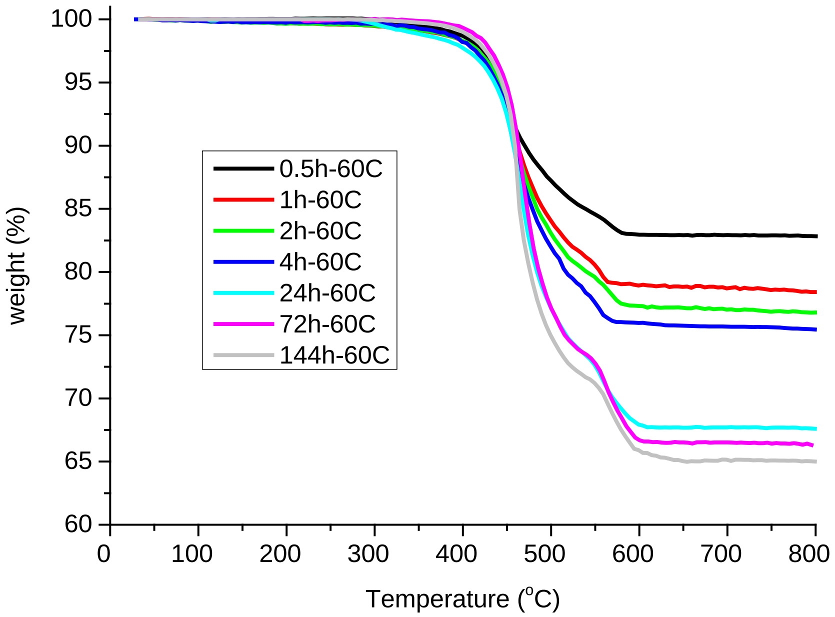

Figure S7. Thermogravimetric analysis of ZnO@ZIF-8 composite microspheres prepared in the presence of C_{12}Gua in MeOH at 60 °C for various reaction times.

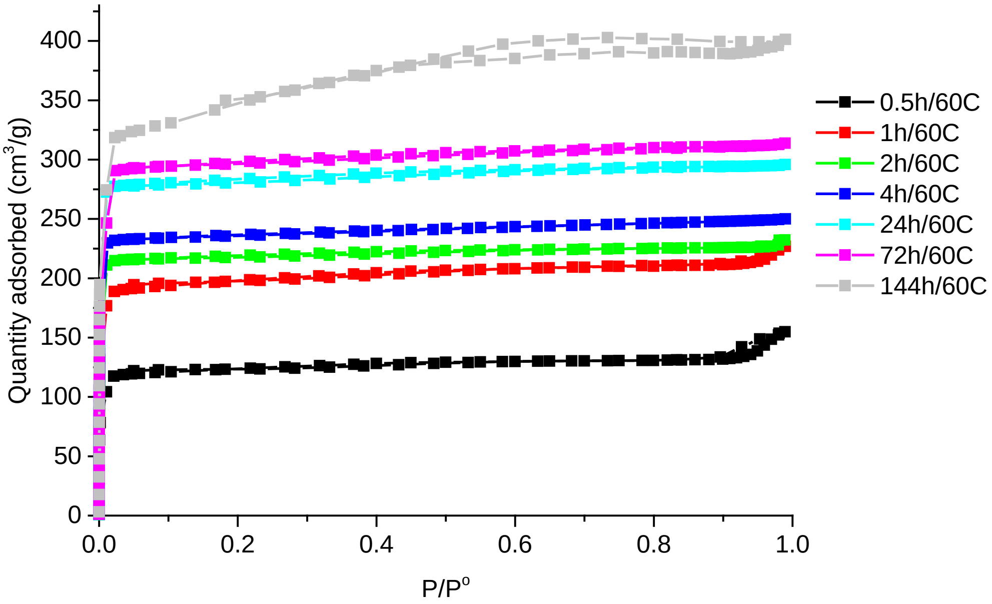

Figure S8. Nitrogen adsorption isotherm (77 K) of ZnO@ZIF-8 composite microspheres prepared in the presence of C_{12}Gua in MeOH at 60 °C for various reaction times.

Sample	S_{BET}(m^2/g)	Micropore Vol (cm^3/g)[a]	Organic content from TGA (wt%)	Residual ZnO content (wt%)	ZIF-8 %	ZnO %
ZnO@ZIF-0.5h	509	0.19	17.2	82.8	26.9	73.1
ZnO@ZIF-1h	806	0.30	21.6	78.4	33.7	66.3
ZnO@ZIF-2h	978	0.33	23.2	76.8	36.2	63.8
ZnO@ZIF-4h	1017	0.36	24.6	75.4	38.4	61.6
ZnO@ZIF-24h	1225	0.44	32.4	67.6	50.6	49.4
ZnO@ZIF-72h	1245	0.46	33.7	66.3	52.6	47.4
ZnO@ZIF-144h	1372	0.52	35	65	54.7	45.3

[a] Maximum pore volume at P/Po = 0.17 determined by the Horvath-Kawazoe method.

Table S2. Porosity and composition data of ZnO@ZIF-8 composite microspheres prepared in the presence of C_{12}Gua in MeOH at 60 °C for various reaction times. The composition is determined from the TGA data in figure S7 and the BET surface areas from the isotherms in figure S8.

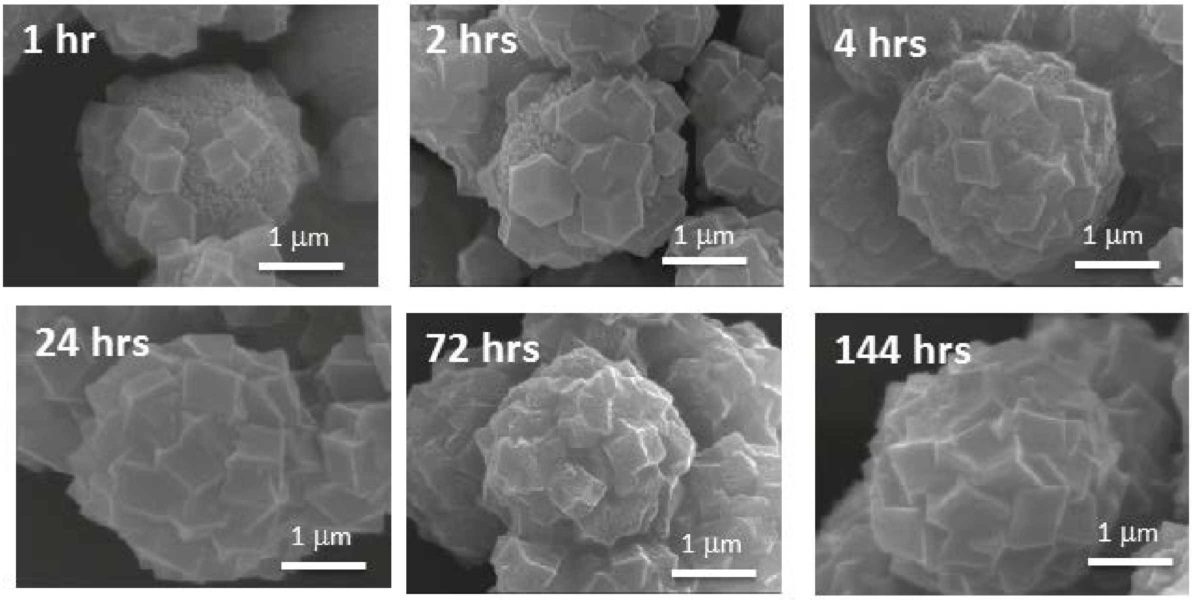

Figure S9. SEM images of ZnO@ZIF-8 composite microspheres prepared in the presence of C_{12}Gua in MeOH at 60 °C for various reaction times.

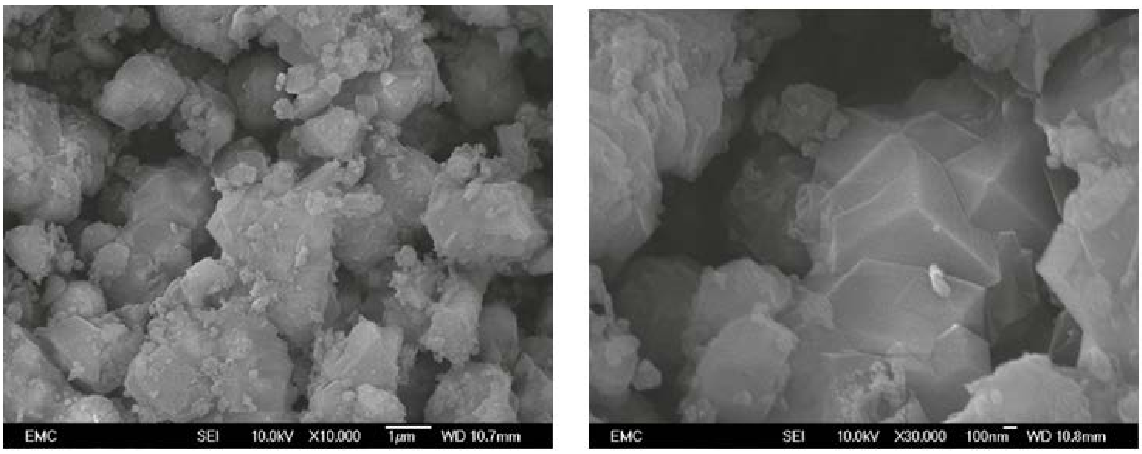

Figure S10. SEM images following conversion of ZnO microspheres in the presence of MeIm without the addition of C_{12}Gua in MeOH at 60 °C. It is clear that the microspherical shape is lost in the absence of the amphiphile.

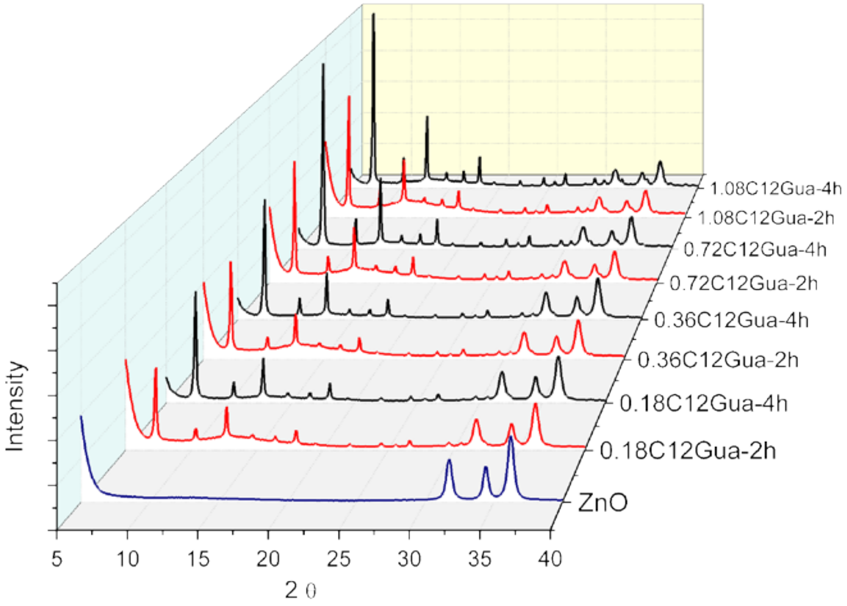

Figure S11. PXRD data of ZnO@ZIF-8 composite microspheres prepared in MeOH at 60 °C using various amounts of added C_{12}Gua (cf. the standard synthesis conditions of 0.27 mmol C_{12}Gua). Reactions were conducted for 2 hrs and 4 hrs duration at each C_{12}Gua concentration.

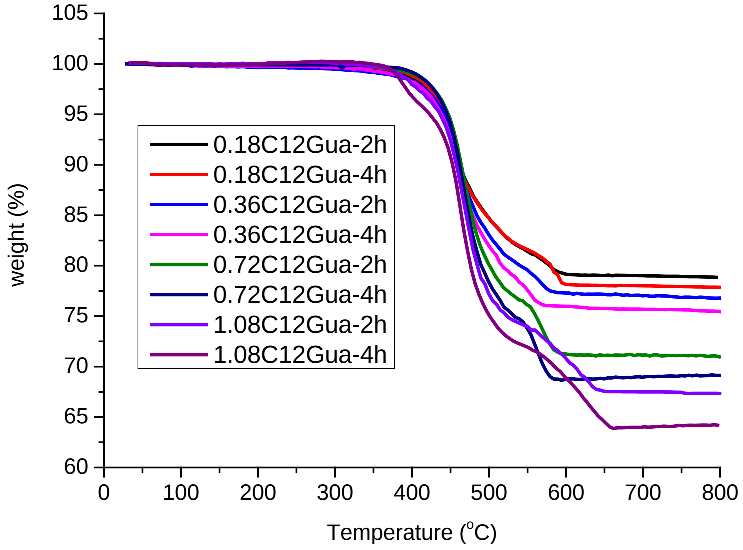

Figure S12. Thermogravimetric analysis of ZnO@ZIF-8 composite microspheres prepared in MeOH at 60 °C using various amounts of added C_{12}Gua.

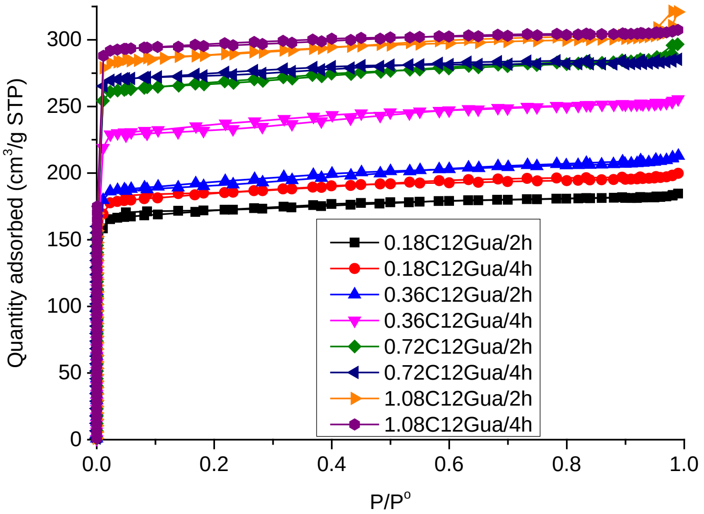

Figure S13. Nitrogen adsorption isotherms (77 K) of ZnO@ZIF-8 composite microspheres prepared in MeOH at 60 °C using various amounts of added C_{12}Gua.

Sample	S_{BET}(m^2/g)	Organic content from TGA (wt%)	Residual ZnO content (wt%)	ZIF-8 %	ZnO %
0.18C12Gua-2h	723	20.9	78.8	32.6	67.4
0.18C12Gua-4h	776	22.0	77.9	34.4	65.6
0.36C12Gua-2h	816	22.8	76.8	35.6	64.4
0.36C12Gua-4h	1008	24.3	75.6	38.0	62.0
0.72C12Gua-2h	1148	28.9	70.1	45.1	54.9
0.72C12Gua-4h	1220	30.8	69.0	48.1	51.9
1.08C12Gua-2h	1247	32.6	67.0	51.0	49.0
1.08C12Gua-4h	1289	35.8	64.0	56.0	44.0

Table S3. Porosity and composition data of ZnO@ZIF-8 composite microspheres prepared in in MeOH at 60 °C using various amounts of added C_{12}Gua. The composition is determined from the TGA data in figure S12 and the BET surface areas from the isotherms in figure S13.

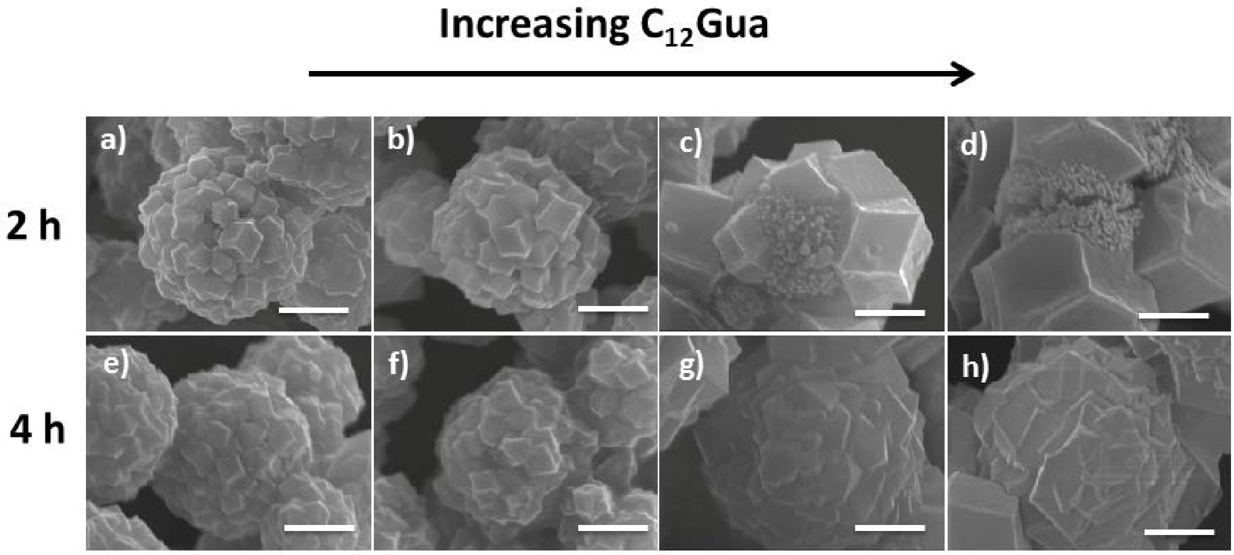

Figure S14. SEM images of ZnO@ZIF-8 composite microspheres prepared in MeOH at 60 °C using various amounts of added C_{12}Gua for 2 and 4 hrs of reaction. (a, e) 0.18 mmol; (b, f) 0.36 mmol; (c, g) 0.72 mmol; (d, h) 1.08 mmol. Scale bar in all images is 1µm.

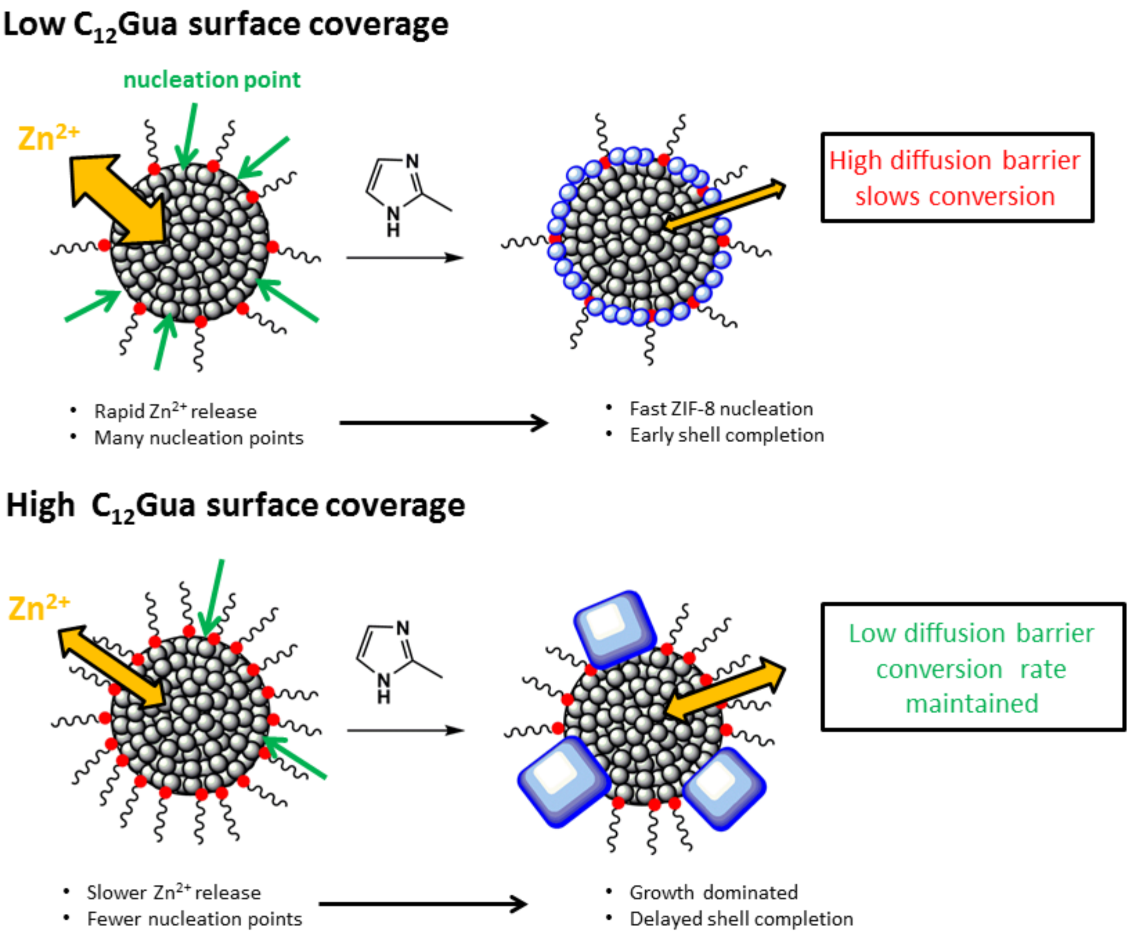

Figure S15. Schematic representation of the proposed oxide surface passivation mechanism in the presence of C_{12}Gua.

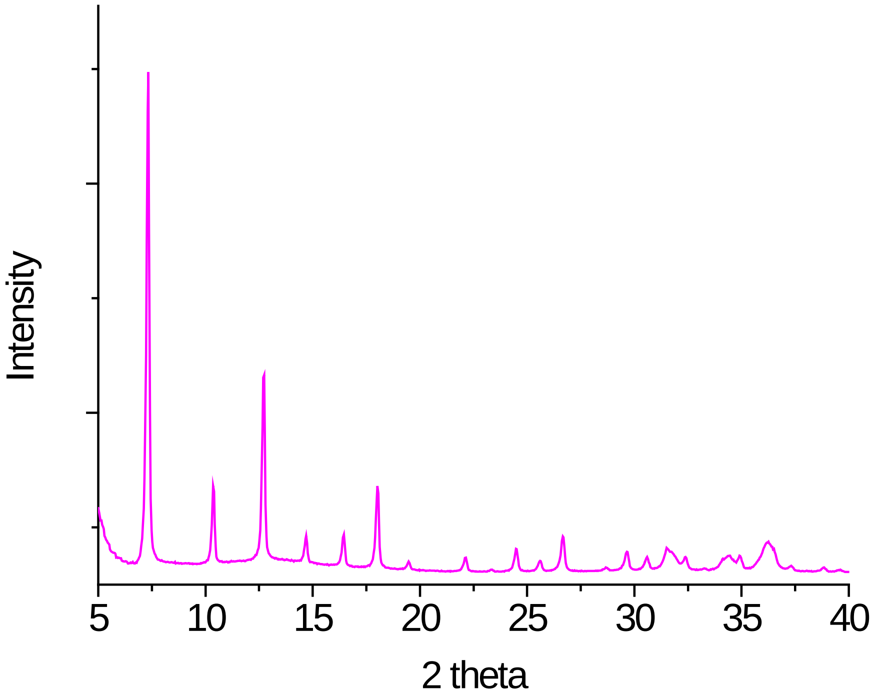

Figure S16. PXRD following conversion of ZnO microspheres in the presence of MeIm without the addition of C_{12}Gua in MeOH.

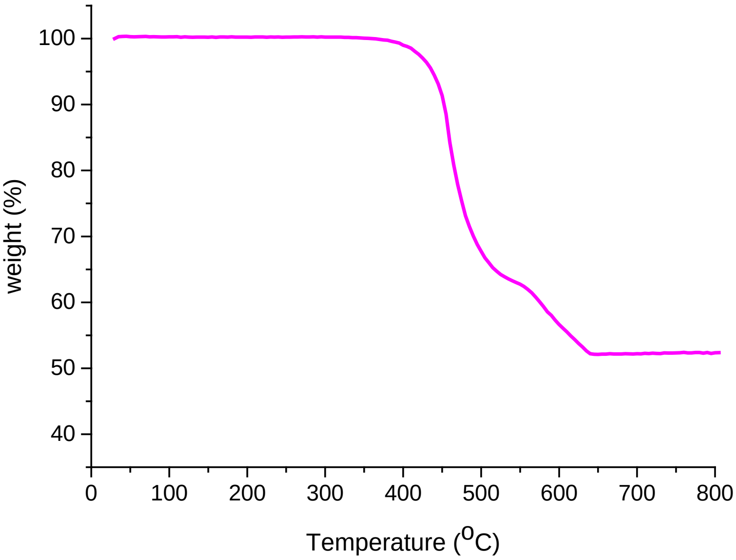

Figure S17. Thermogravimetric analysis following conversion of ZnO microspheres in the presence of MeIm without the addition of C_{12}Gua in MeOH. The organic mass loss is consistent with a conversion level of ZnO to ZIF-8 of 80%.

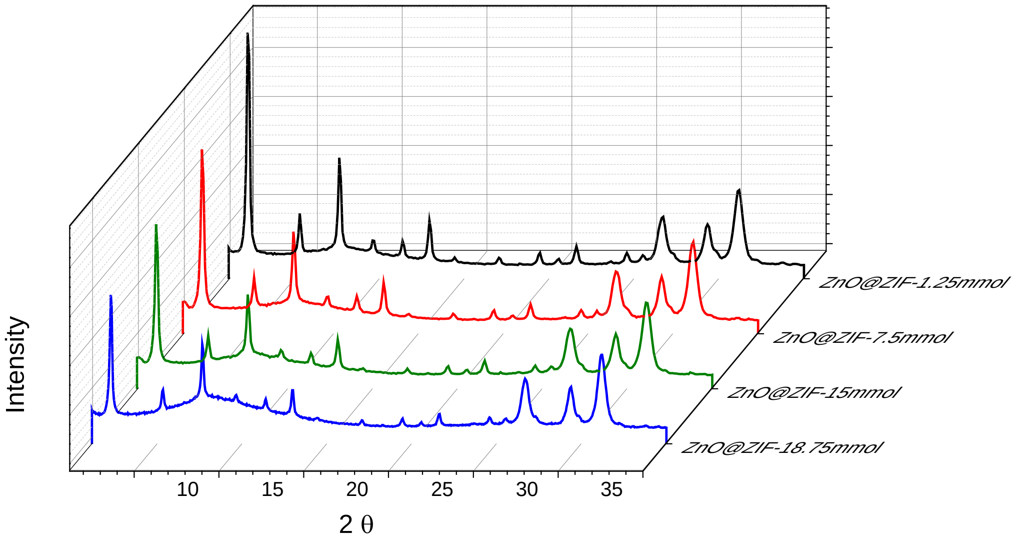

Figure S18. PXRD data of ZnO@ZIF-8 composite microspheres prepared in the presence of C_{12}Gua at 60 °C in MeOH using various amounts of added MeIm. The standard synthesis condition is 18.75 mmol of MeIm, shown by the blue diffractogram.

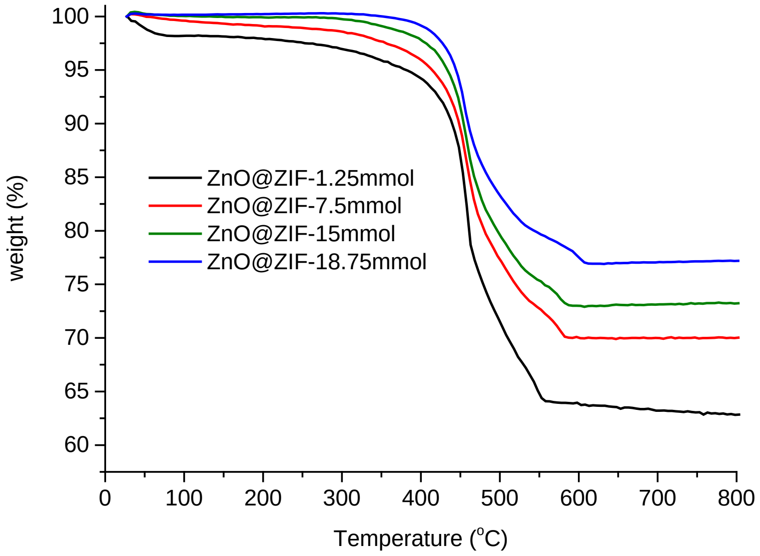

Figure S19. Thermogravimetric analysis of ZnO@ZIF-8 composite microspheres prepared in the presence of C_{12}Gua at 60 °C in MeOH using various amounts of added MeIm, demonstrating that the organic mass loss and thus conversion to ZIF-8 increases as the amount of MeIm is reduced.

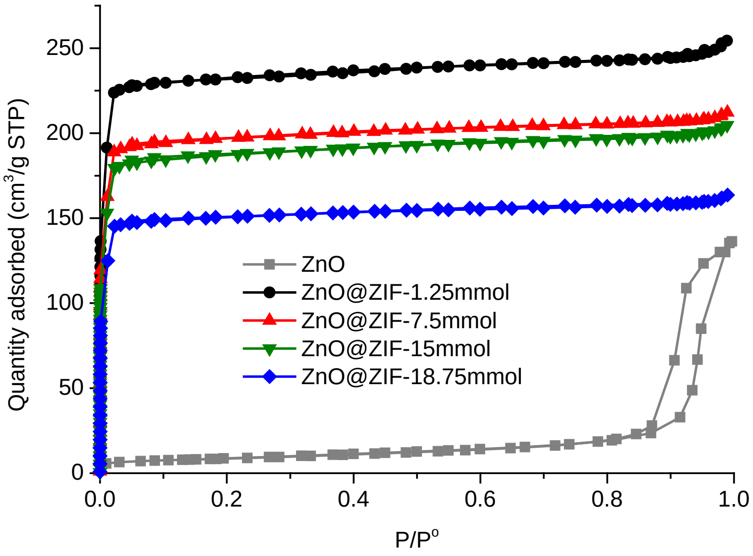

Figure S20. Nitrogen adsorption isotherms (77 K) of ZnO@ZIF-8 composite microspheres prepared in the presence of C$_{12}$Gua at 60 °C in MeOH using various amounts of added MeIm compared to the starting ZnO. Increasing uptake with decreased MeIm in the reaction confirms the increased ZIF-8 conversion under these conditions.

ZnO@ZIF-8-mmol of MeIm	**S_{BET} (m^2/g)**	**Micropore Vol (cm^3/g)[a]**	**Organic content from TGA (wt%)**	**Residual ZnO content (wt%)**	**Starting decomposition (^{o}C)**	**ZIF-8%**	**ZnO%**
ZnO@ZIF-8-1.25mmol	958	0.36	35.04	62.84	200	54.75	45.25
ZnO@ZIF-8-7.5mmol	765	0.29	28.91	70.0	250	45.17	54.83
ZnO@ZIF-8-15mmol	735	26.5	26.5	73.23	300	41.4	58.6
ZnO@ZIF-8-18.75mmol	616	0.23	22.72	77.18	330	35.5	64.5

[a] Maximum pore volume at P/Po = 0.17 determined by the Horvath-Kawazoe method.

Table S4. Porosity and composition data of ZnO@ZIF-8 composite microspheres prepared in the presence of C$_{12}$Gua at 60 °C in MeOH using various amounts of added MeIm. The composition is determined from the TGA data in figure S19 and the BET surface areas from the isotherms in figure S20.

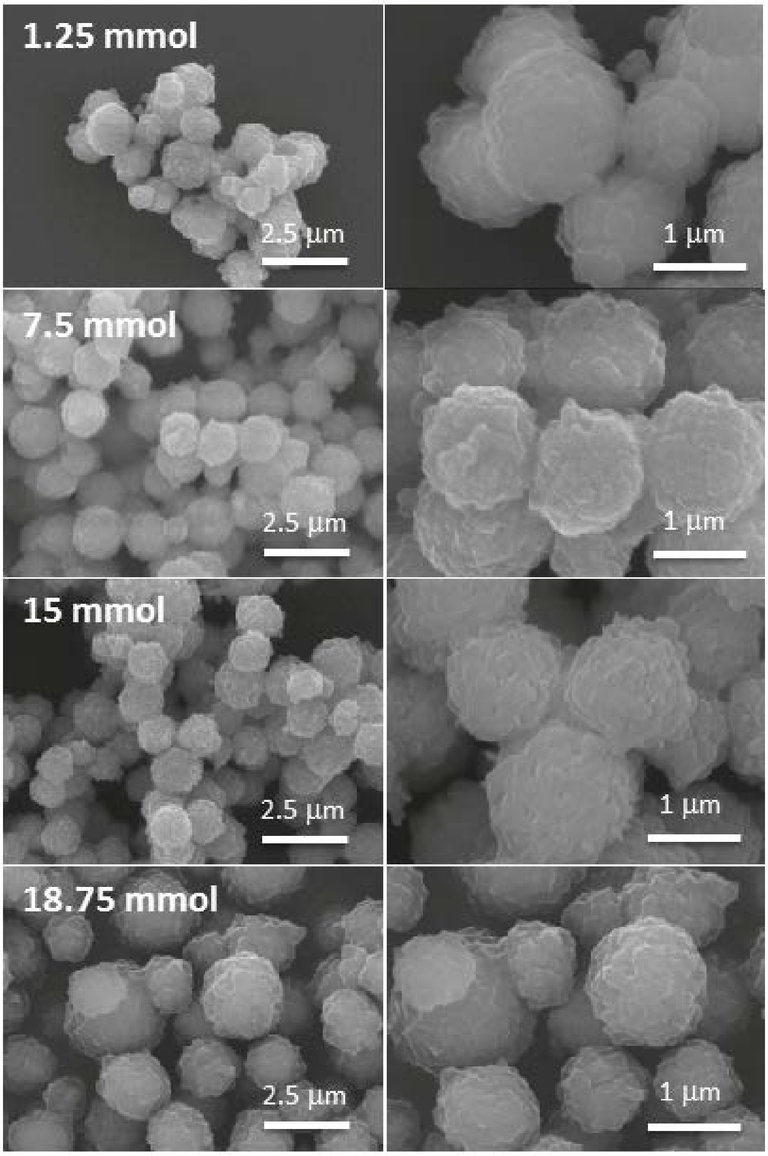

Figure S21. SEM images of ZnO@ZIF-8 composite microspheres prepared in the presence of C_{12}Gua at 60 °C in MeOH using various amounts of added MeIm.

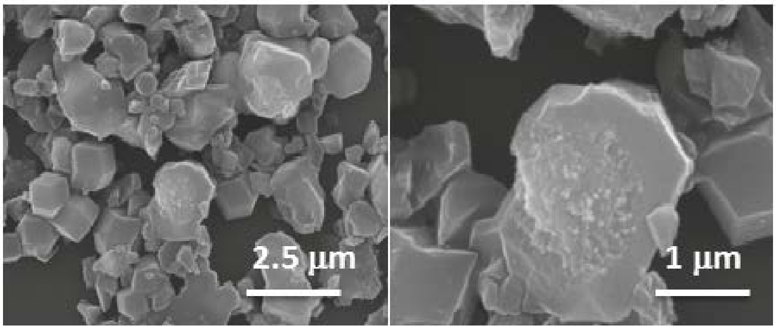

Figure S22. SEM images following conversion of ZnO microspheres to ZIF-8 in the presence of CTAB in MeOH at r.t., demonstrating the loss of the microspherical shape of the oxide template.

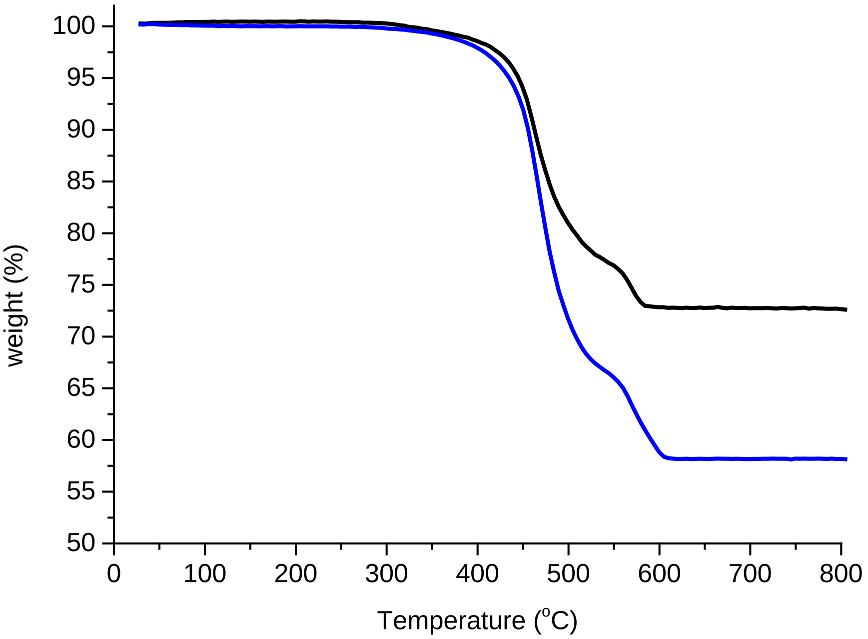

Figure S23. Thermogravimetric analysis of ZnO@ZIF-8 composites prepared using C_{12}Gua (black) and CTAB (blue). The organic mass losses indicate that ZnO conversion to ZIF-8 is 43% for C_{12}Gua and 68% for CTAB, the latter more closely resembling those results obtained in the absence of surfactant shown in figures S17.

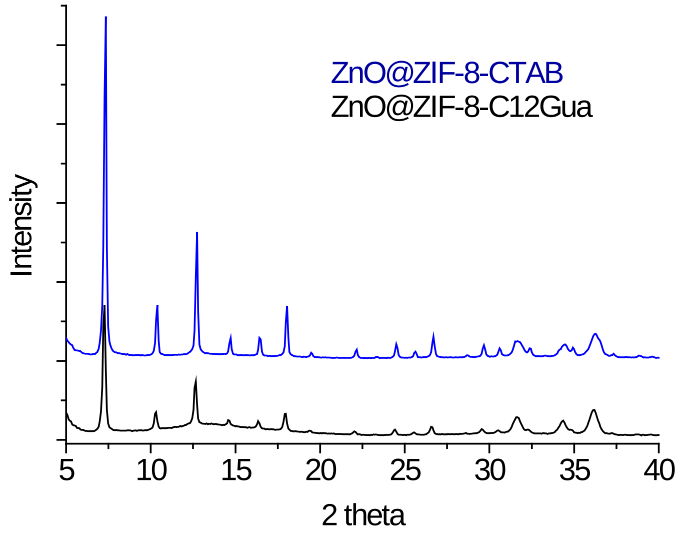

Figure S24. PXRD data of ZnO@ZIF-8 composites prepared using C_{12}Gua and CTAB.

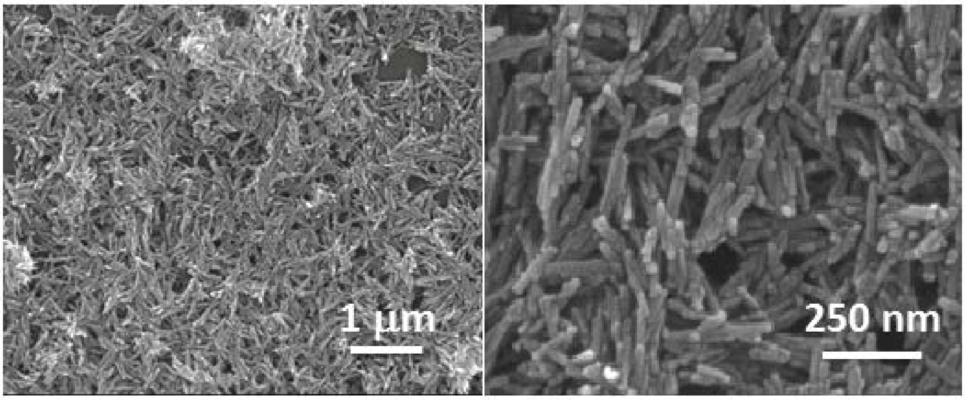

Figure S25. SEM images of as-prepared ZnO nanowire templates.

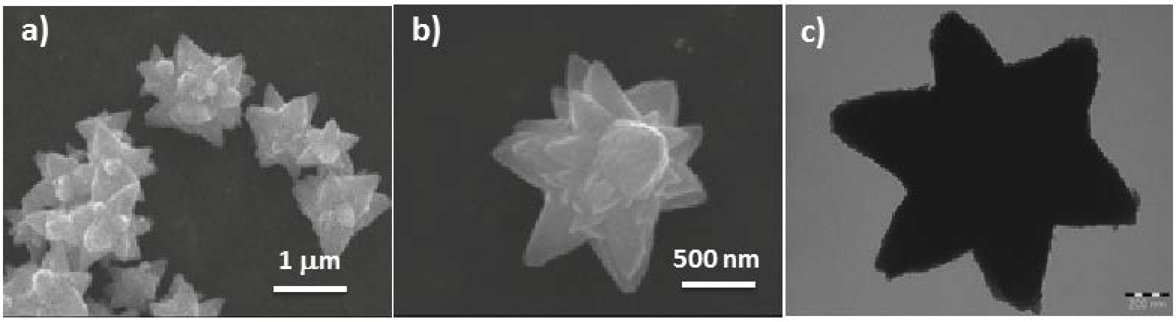

Figure S26. (a, b) SEM images and (c) TEM image of as-prepared ZnO star-shaped templates. Scale bar in (c) = 200 nm.

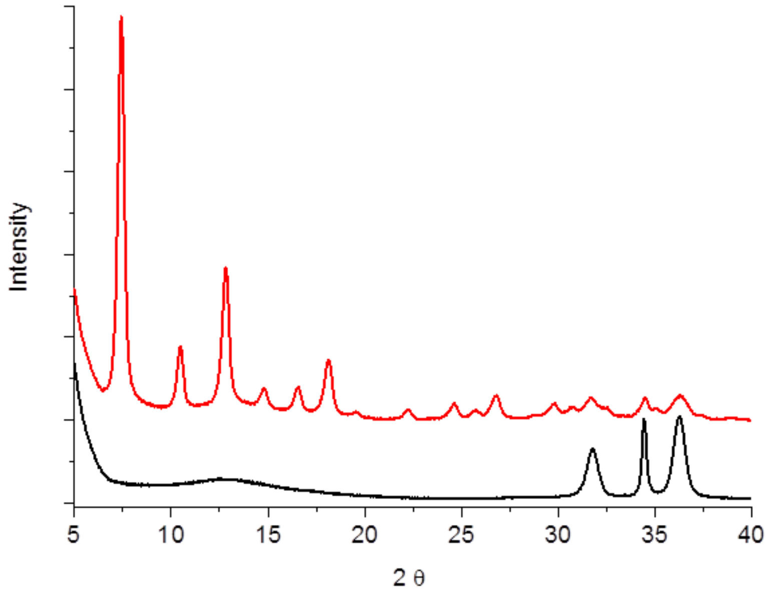

Figure S27. PXRD data of nanowire ZnO (black) and the corresponding ZnO@ZIF-8 composites (red) following reaction with MeIm at 60 °C in the presence of C_{12}Gua. The broadened peaks associated with the oxide result from its downsizing to the nanoscale.

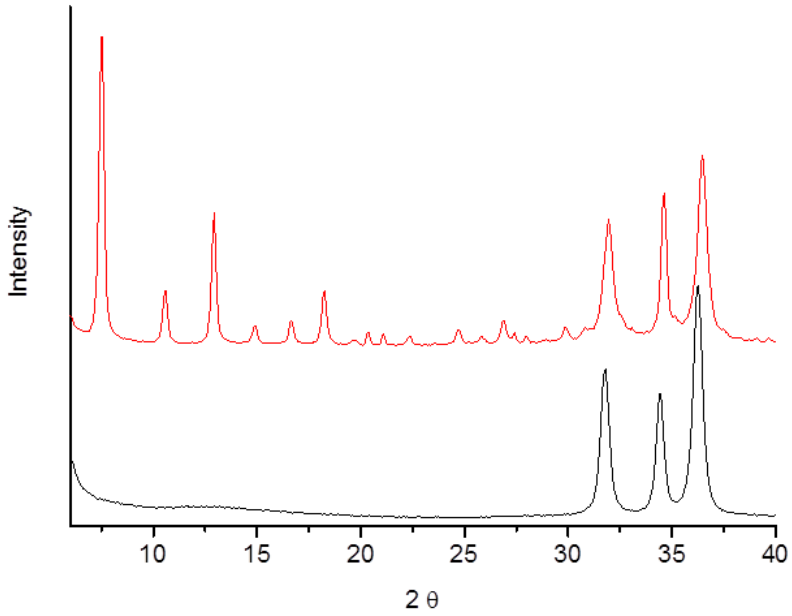

Figure S28. PXRD data of star-shaped ZnO (black) and the corresponding ZnO@ZIF-8 composites (red) following reaction with MeIm at 60 °C in the presence of C_{12}Gua. It is likely that the greater proportion of ZnO remaining in this composite compared to the nanowires arises from the reduced surface/bulk ratio of the star-shaped templates.

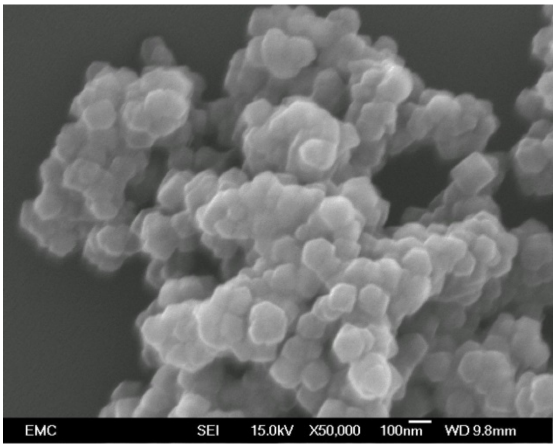

Figure S29. SEM image of the ZnO@ZIF-8 composite prepared from ZnO nanospheres in MeOH in the presence of C_{12}Gua. Compare this to the well-defined core-shell structures that are accessible by reaction in water as shown in figure S2.

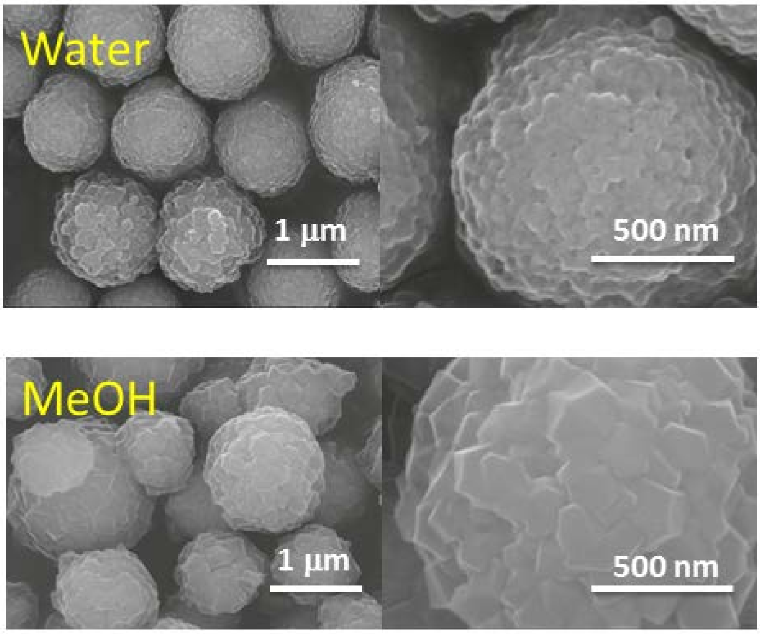

Figure S30. SEM images of ZnO@ZIF-8 composite microspheres prepared in the presence of C_{12}Gua in water and MeOH for 3 days at 60 °C.

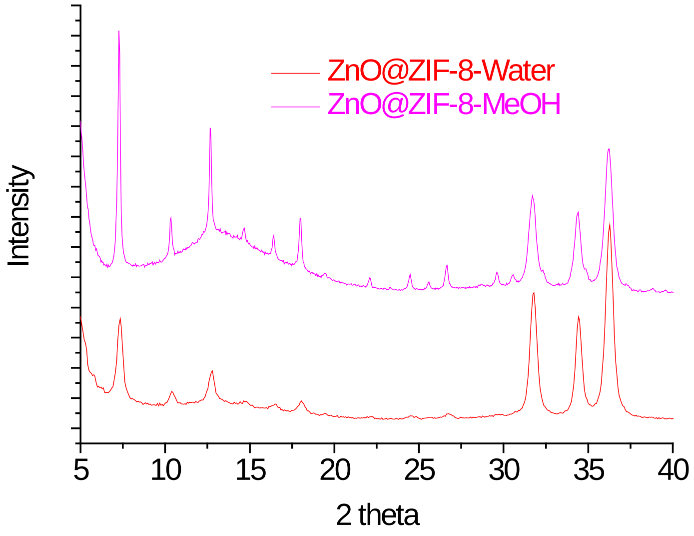

Figure S31. PXRD data of ZnO@ZIF-8 composite microspheres prepared in the presence of C_{12}Gua in water and MeOH for 3 days at 60 °C.

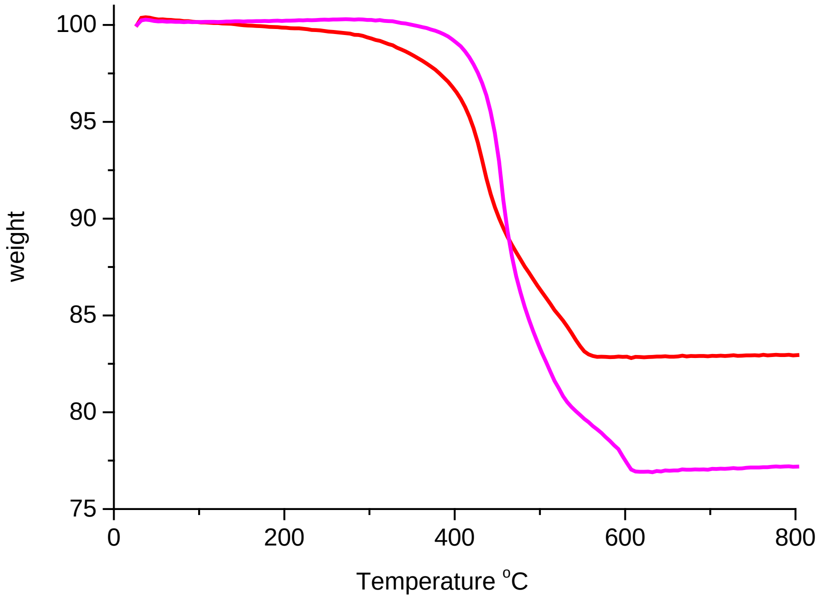

Figure S32. Thermogravimetric analysis of ZnO@ZIF-8 composite microspheres prepared in the presence of C_{12}Gua in water (red) and MeOH (pink) for 3 days at 60 °C. The organic mass losses indicate that conversion of ZnO to ZIF-8 is 26.1% when the reaction is conducted in water and 36% in MeOH.

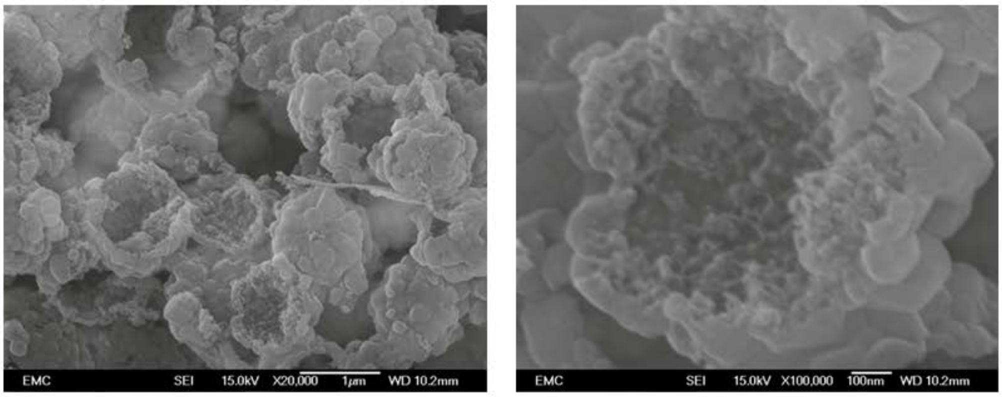

Figure S33. SEM images of hollow ZIF-8 capsules after selective etching of the ZnO core from ZnO@ZIF-8 core-shell composite microspheres with 2M KOH. The ZnO@ZIF-8 microspheres are pre-coated in PVP which permits the spherical shape to be retained during the etching process.

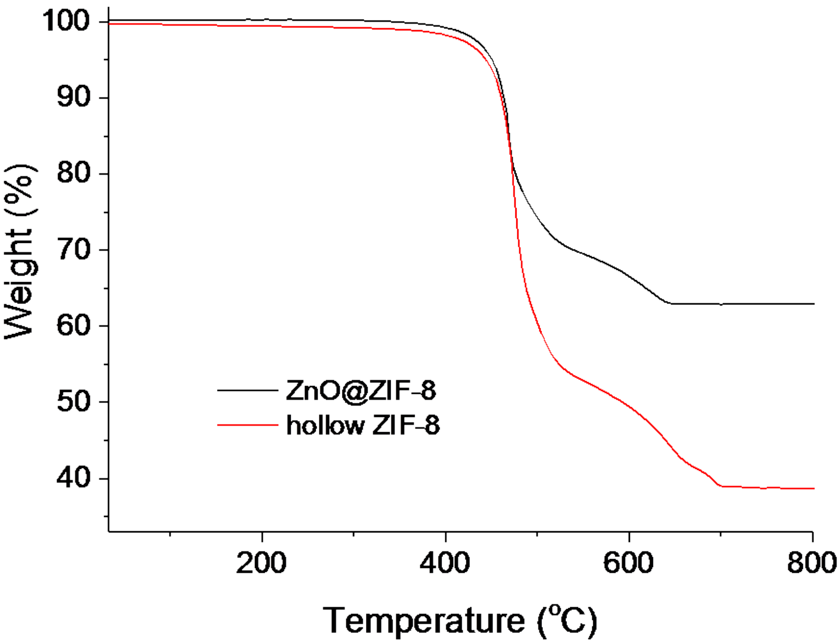

Figure S34. Thermogravimetric analysis of as-prepared ZnO@ZIF-8 composite microspheres (black) and the resulting ZIF-8 hollow capsules (red) following etching of the core with KOH. The residual ZnO mass observed for hollow ZIF-8 is 37.5 wt%, which is in excellent agreement with that calculated for bulk ZIF-8 (36 wt%). This indicates that the ZnO core is almost completely etched away using this method.

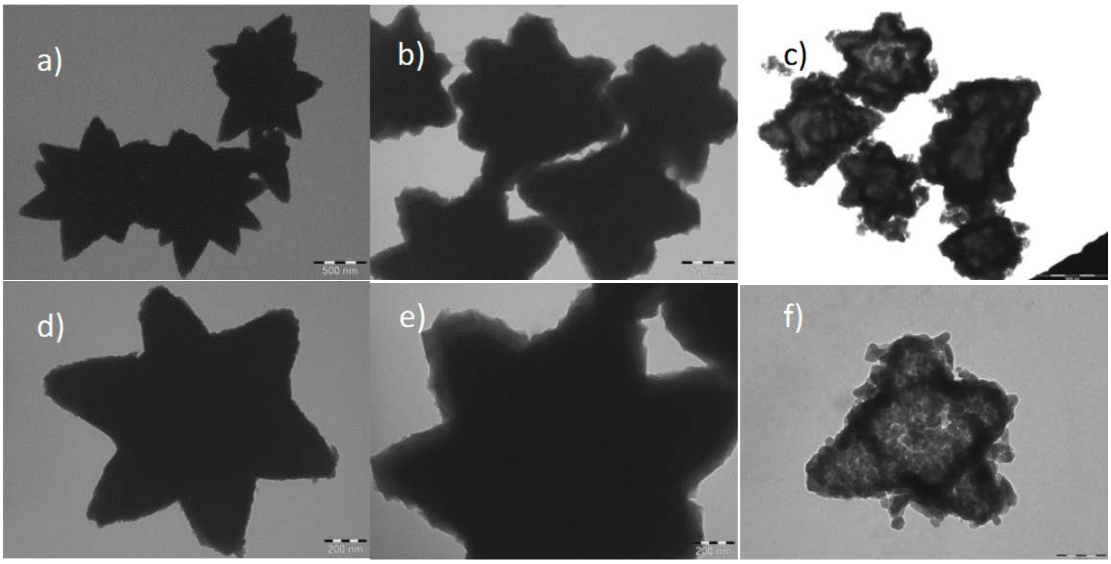

Figure S35. TEM images of (a, d) star-shape ZnO; (b, e) star-shape ZnO@ZIF-8 composites and (c, f) hollow star-shape ZIF-8 obtained following etching of the ZnO core with KOH.

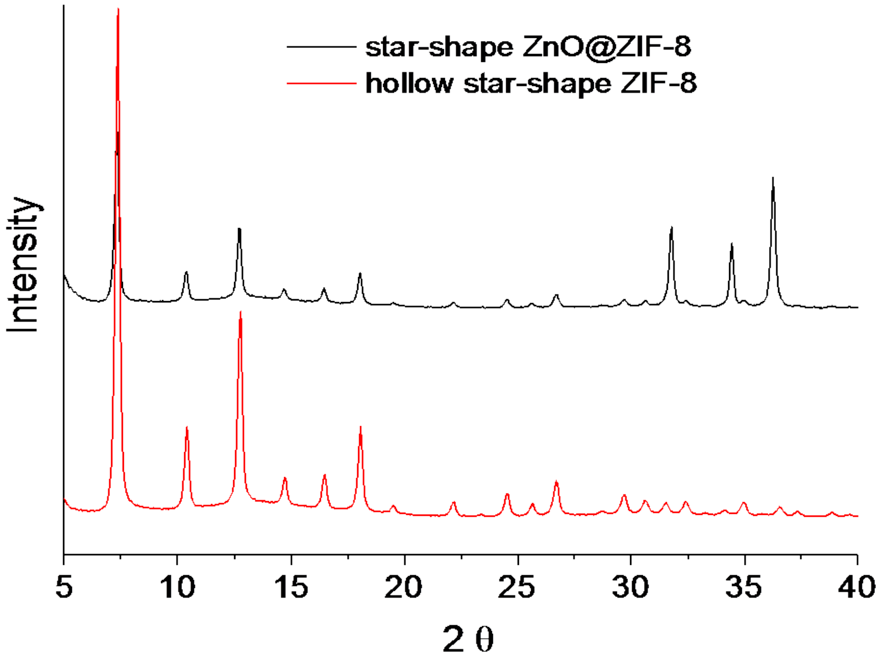

Figure S36. PXRD data of star-shaped ZnO@ZIF-8 composites (black) and the resulting hollow ZIF-8 (red) after etching of the ZnO core with KOH.

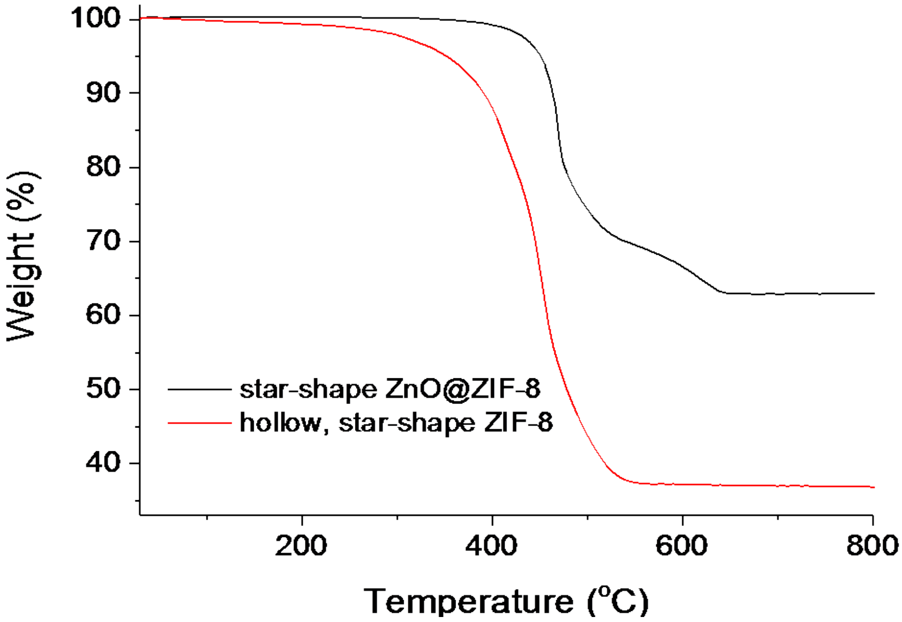

Figure S37. Thermogravimetric analysis of star-shaped ZnO@ZIF-8 composites (black) and the resulting hollow ZIF-8 (red) after etching of the ZnO core with KOH. The organic mass loss and residual ZnO for the hollow star-shaped ZIF-8 are in excellent agreement with the bulk phase.

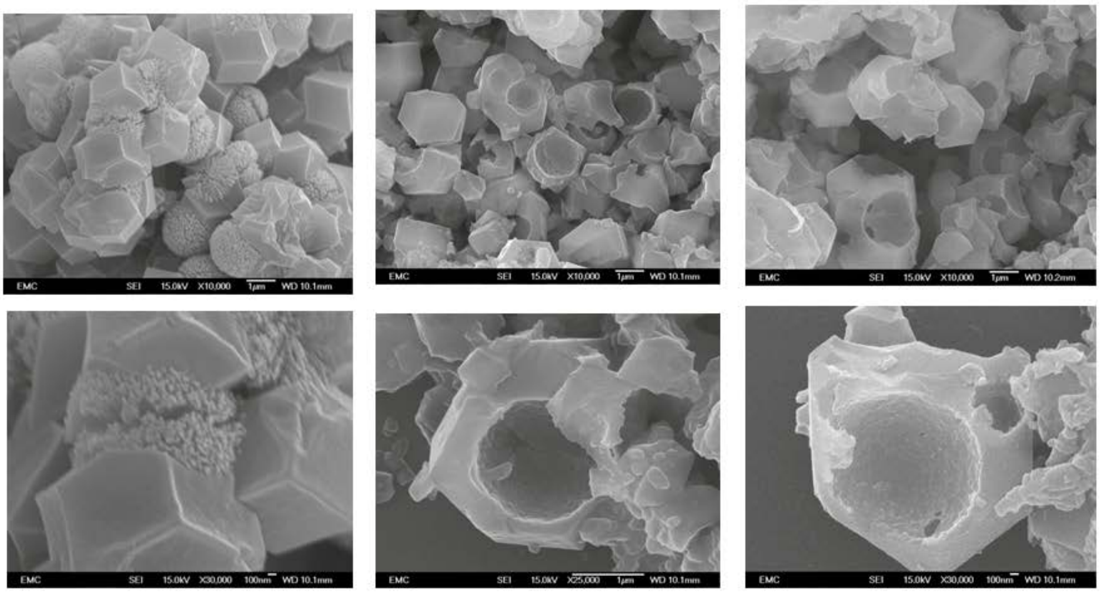

Figure S38. SEM images of ZIF-8 bowl-like crystals (middle and right) following etching of the ZnO component from samples prepared using high levels of C_{12}Gua (left).

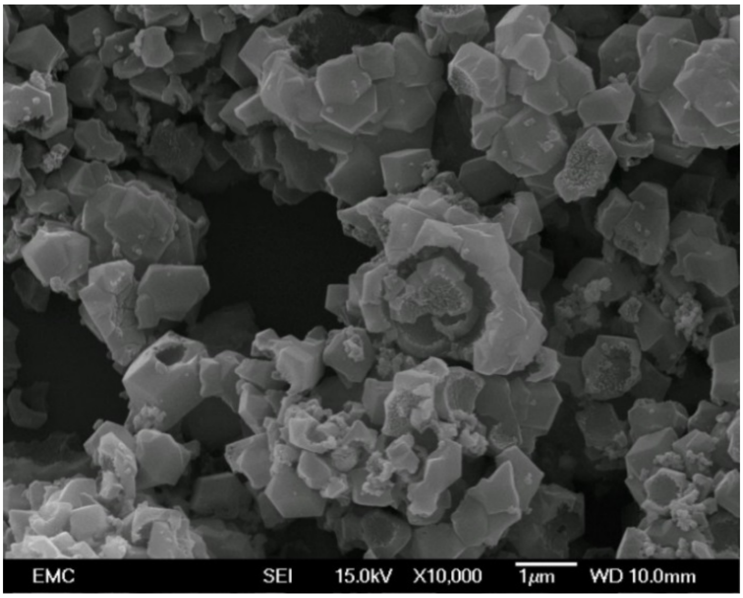

Figure S39. SEM image of ZIF-8 following etching of the core from ZnO@ZIF-8 composite microspheres in the absence of PVP. The spherical structure is largely lost and the sample is dominated by free ZIF-8 crystals indicating the importance of PVP in retaining shape and protecting the shell during etching.

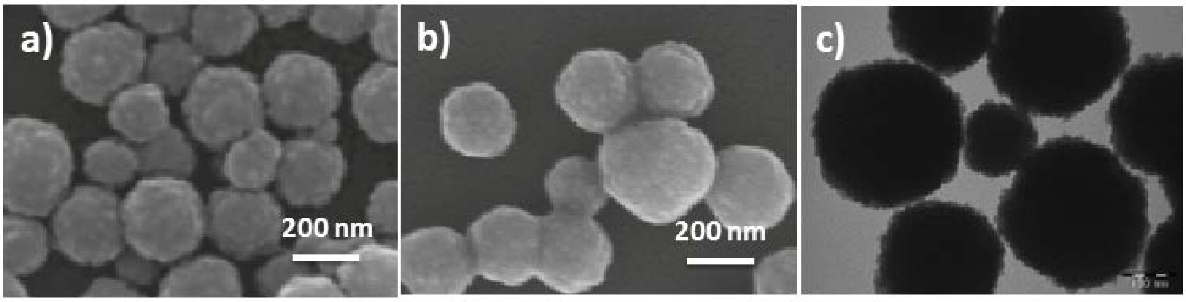

Figure S40. SEM images of (a) Fe_3O_4 nanospheres and (b) Fe_3O_4@ZnO templates following coating of the former in a shell of ZnO. (c) TEM image of Fe_3O_4@ZnO, scale bar = 100 nm.

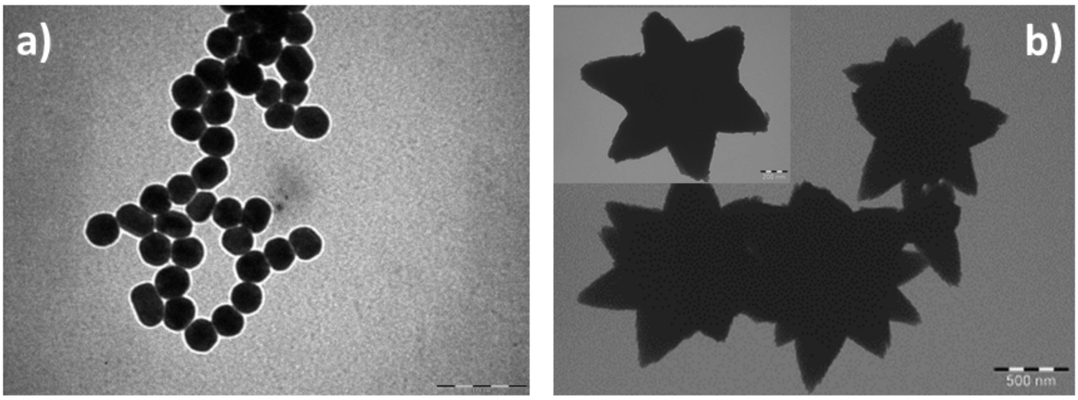

Figure S41. TEM images of (a) 40 nm Au NPs and (b) star-shaped AuNP@ZnO templates following coverage of the Au particles in the desired morphology of ZnO.

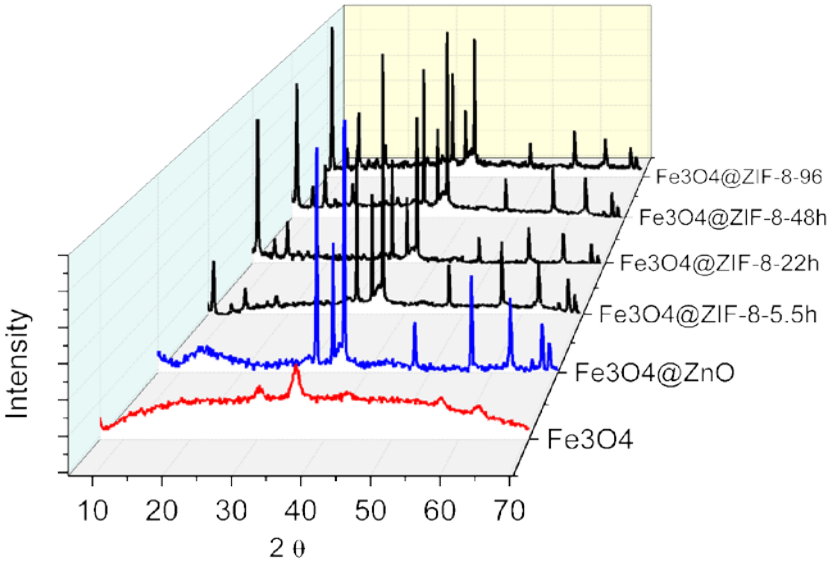

Figure S42. PXRD data of Fe_3O_4@ZnO@ZIF-8 ternary composites prepared by the aqueous reaction of Fe_3O_4@ZnO nanospheres with MeIm in the presence of C_{12}Gua for various times. It is clear that all components are present in the composites and that not all of the ZnO is transformed to ZIF-8 in agreement with earlier studies where only ZnO (rather than Fe_3O_4@ZnO) templates were employed with C_{12}Gua.

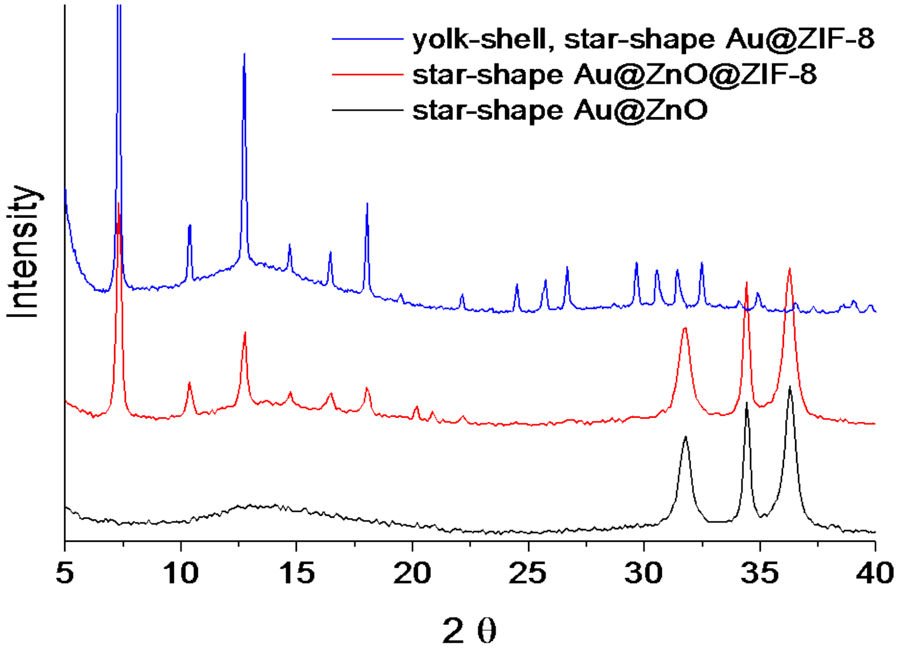

Figure S43. PXRD data of star-shaped Au@ZnO templates (black), the ternary AuNP@ZnO@ZIF-8 composite following reaction with MeIm with C12Gua in water (red) and the resulting AuNP@ZIF-8 yolk-shell architecture (blue) following selective etching of the oxide component with KOH.

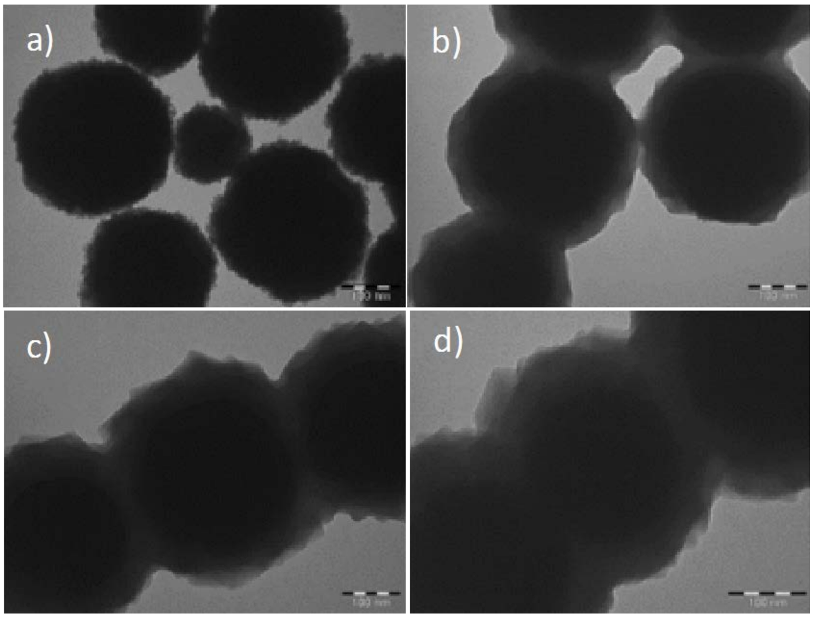

Figure S44. TEM images of Fe_3O_4@ZnO particles and Fe_3O_4@ZnO@ZIF-8 composites obtained after (b) 6h; (c) 24h and (d) 48 h reaction with MeIm in the presence of C_{12}Gua. The increasing thickness of the ZIF-8 shell is an agreement with the PXRD shown in figure S42.

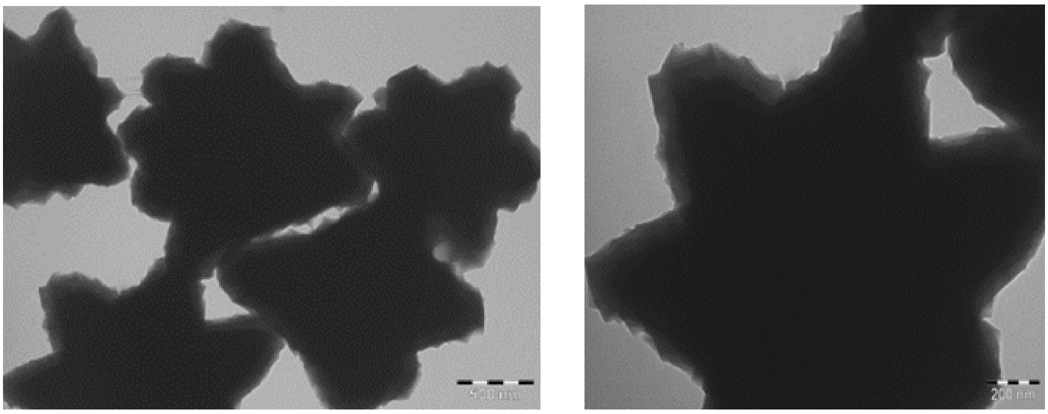

Figure S45. TEM images of star-shaped AuNP@ZnO@ZIF-8 composites. Scale bars = 500 nm (left image) and 200 nm (right image).

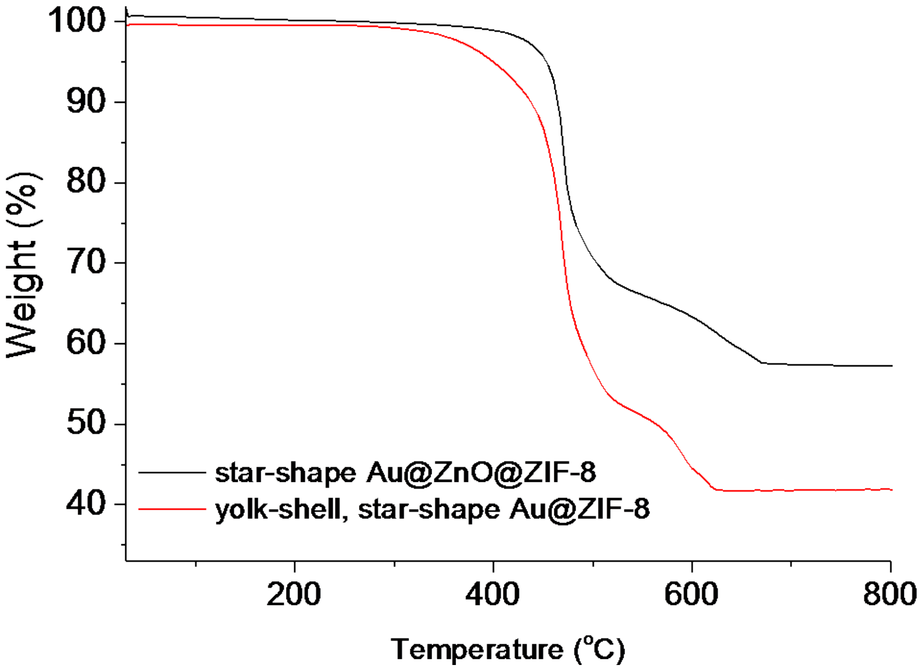

Figure S46. Thermogravimetric analysis of star-shaped AuNP@ZnO@ZIF-8 (black) and the resulting AuNP@ZIF-8 yolk shell structure (red) following etching with KOH. The residual masses indicate that the composite contains 65 wt% ZIF-8, 6 wt% Au and 29% ZnO.

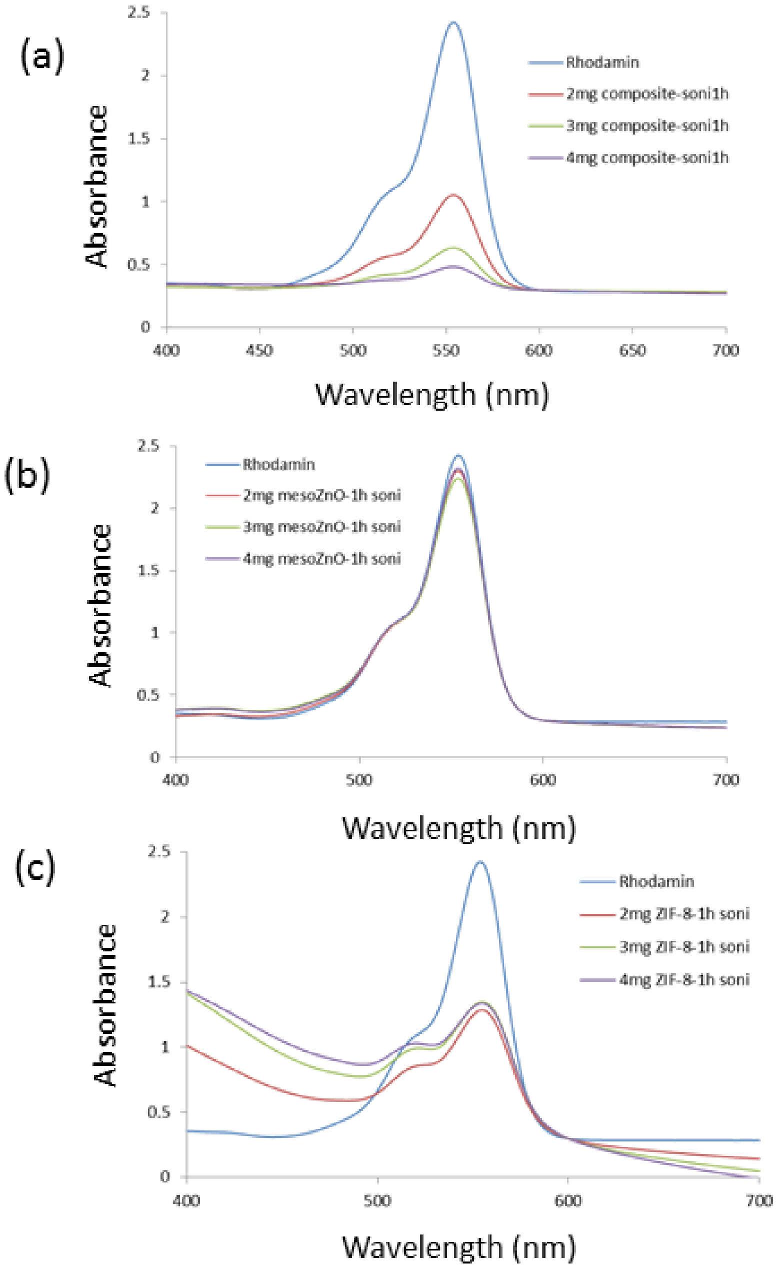

Figure S47. Removal of RhB from an aqueous solution (10 mg/L, 0.02 mM) following addition of different amounts of (a) ZnO@ZIF-8 composite microspheres, (b) ZnO and (c) ZIF-8.

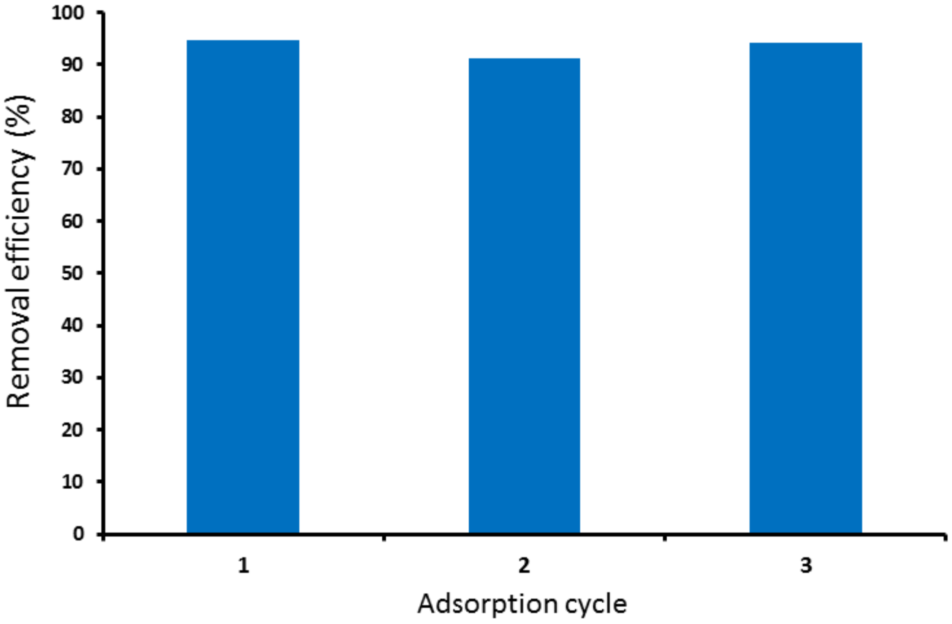

Figure S48. Recyclability of ZnO@ZIF-8 microspheres for RhB removal from aqueous RhB/MV^{2+} mixtures.

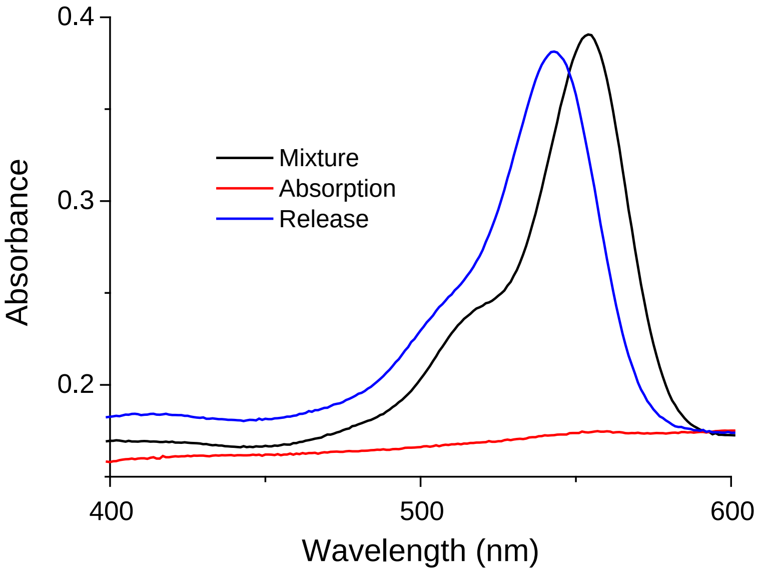

Figure S49. UV-vis absorption data showing uptake and release of RhB from a 1:100 mixture of RhB to methyl viologen, demonstrating the high affinity RhB has for the surface of the ZnO@ZIF-8 composite microspheres.

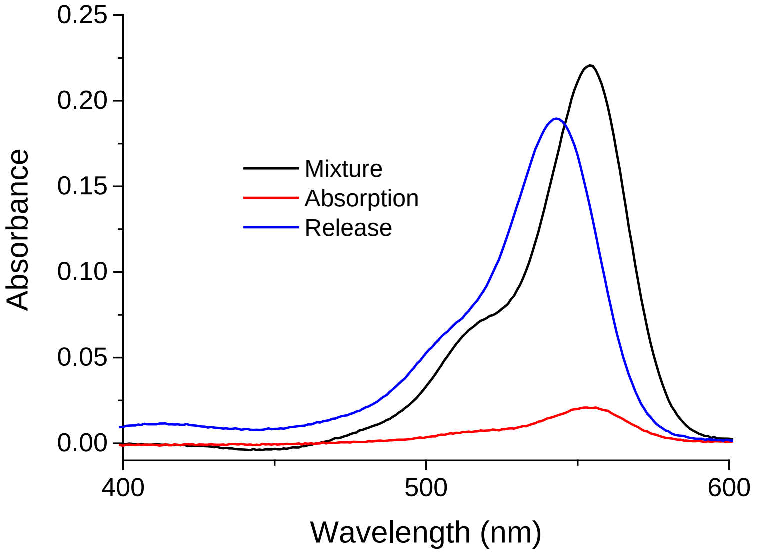

Figure S50. UV-vis absorption data showing uptake and release of RhB from a 1:100 mixture of RhB to methyl viologen using the Fe_3O_4@ZnO@ZIF-8 composite microspheres.

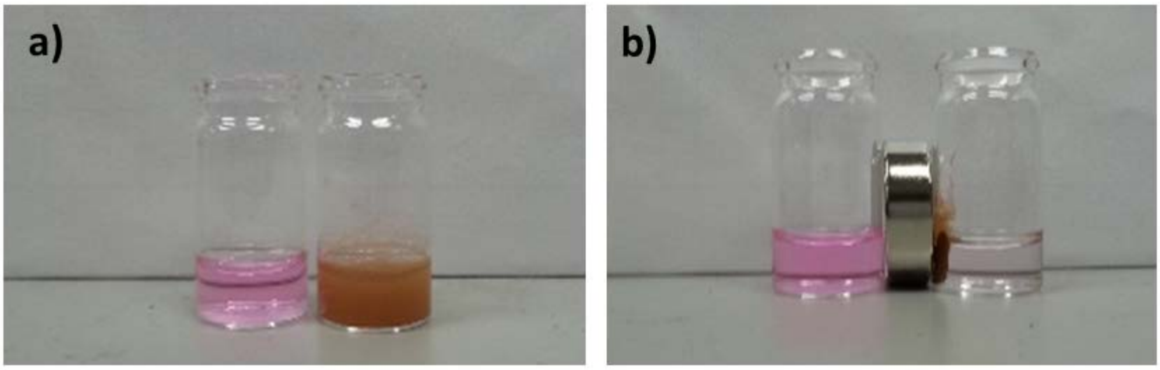

Figure S51. (a) Adsorption of RhB from 1:100 mixture of RhB to methyl viologen using Fe_3O_4@ZnO@ZIF-8 composite microspheres. (b) Magnetic recovery of the composite for effective separation of RhB from dye mixtures.

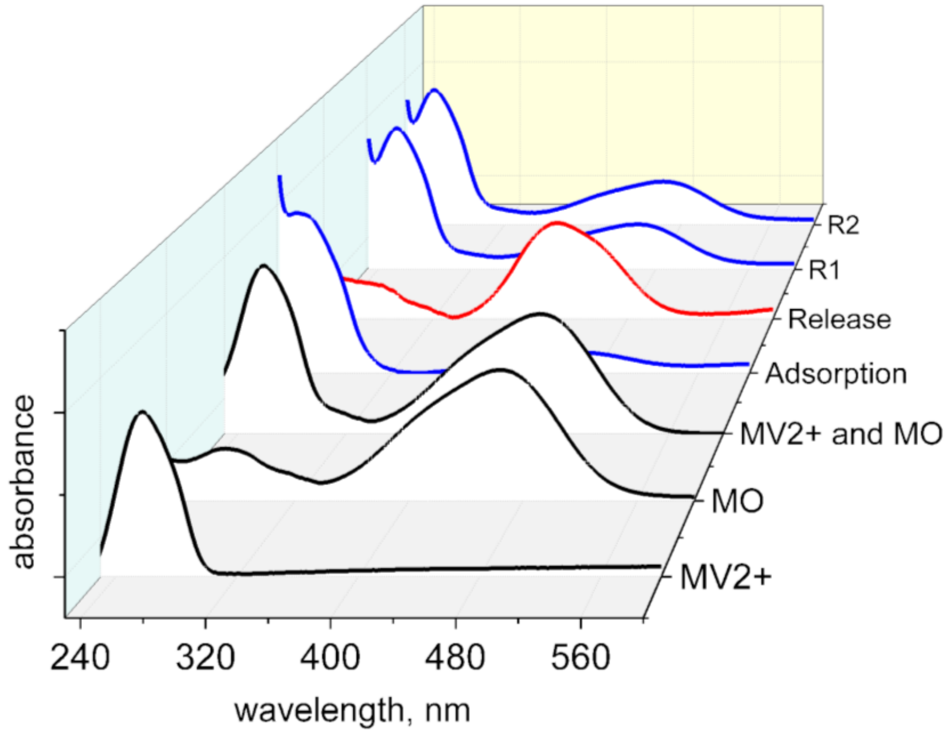

Figure S52. UV-Vis absorption spectra demonstrating selective adsorption of MO over MV^{2+} from aqueous solution, and showing the recovery of MO following release from the composite surface with EtOH. The second and third MO adsorption cycles are denoted R1 and R2, which are reduced compared to the first adsorption due to the relative insolubility of MO in EtOH preventing complete release from the previous cycle. The absorption maximum of MO is 464 nm, and the ratio of MO to MV^{2+} is 1:2.

	Rhodamine B	**Methyl Viologen**	**Methyl orange**
Water solubility	20 g/L[a]	620 g/L[b]	5g/L[c]
EtOH solubility	70 g/L[d]	-	Insoluble[c]
Log P_{ow}	1.90[a]	-4.5[b]	1.13[e]

[a]data from *Groundwater* 1999, 37, 376; [b]from http://www.inchem.org/documents/icsc/icsc/eics0005.htm; [c]from http://www.scbt.com/datasheet-206030.html; [d]from http://www.scbt.com/datasheet-203756-rhodamine-b.html; [e]from http://chem.sis.nlm.nih.gov/chemidplus/rn/502-02-3.

Table S5. Dye data table.